

Revisiting the Evolutionary Status of Massive Stars at the central parsec of the Milky Way

A. C. Gormaz-Matamala¹, J. Cuadra^{2,4}, B. Kubátová¹, J. Kubát¹, and S. Ekström³

¹ Astronomický ústav, Akademie věd České republiky, Fričova 298, 251 65 Ondřejov, Czech Republic
e-mail: alex.gormaz@asu.cas.cz

² Departamento de Ciencias, Facultad de Artes Liberales, Universidad Adolfo Ibáñez, Av. Padre Hurtado 750, Viña del Mar, Chile

³ Department of Astronomy, University of Geneva, Chemin Pegasi 51, 1290 Versoix, Switzerland

⁴ Millennium Nucleus on Transversal Research and Technology to Explore Supermassive Black Holes (TITANS), Chile

ABSTRACT

Context. Massive stars and their winds have a large influence in their environment. For example, they determine the accretion rate on to the Galactic Centre (GC) super-massive black hole Sagittarius A* (Sgr A*). The winds of those stars collide and are accreted, at a rate that depends on their chemical composition. Also, the new self-consistent approach to modelling stellar winds of these stars leads to lower mass-loss rates compared to previous standard values, thus altering the stellar properties of their advanced evolutionary stages.

Aims. Here we aim to revisit the evolutionary status of the evolved massive stars at the GC, by means of new tracks based on updated mass-loss rate recipes for the earlier stages of massive stars.

Methods. We use the Geneva-evolution-code (GENEC) for initial stellar masses ranging from 20 to 60 M_{\odot} , for metallicity $Z = 0.020$. We adopt a new mass-loss rate recipe for the line-driven winds of O-type stars and B-supergiants, plus a new recipe for the dust-driven winds of red supergiants (RSG). Additionally, we set up initial rotation $\Omega/\Omega_{\text{crit}} = 0.4$, and we adopt Ledoux criterion for the treatment of convection in inner layers.

Results. We found that evolution models adopting new mass-loss rate prescriptions predict that stars will lose less of their outer layers during their initial phases, while a big reduction of mass happens at the RSG phase. As a consequence, the resulting Wolf-Rayet (WR) stars are less radially homogeneous in their inner structure from the core to the surface. Also, these new evolution models predict the absence of hydrogen-free WN stars. These evolutionary predictions agree better with the observed properties of the WR stars at the GC, in special with their chemical abundances.

Conclusions. We provide a table with the chemical H, He, and CNO abundances calculated for the different subtypes of WR stars (Ofpe/WN9, WNL, WN/C, and WC). We propose a different re-arrangement of the WR subtypes to be used for the modelling of the collision of their winds. We discuss the potential implications of these changes for the colliding winds generated from the massive stars at the GC, which are accreting onto the supermassive black hole Sgr A*.

Key words. Galaxy: Centre – Stars: evolution – Stars: massive – Stars: winds, outflows – Stars: Wolf-Rayet

1. Introduction

Massive stars, born with $M_{\text{zams}} \geq 8 M_{\odot}$, are the hottest and most luminous stars in the Universe. They lose much of their initial mass due to stellar winds and outflows, which are crucial not only for determining the star's final mass, but also for influencing their evolutionary path. These stars are crucial for studying nucleosynthesis, the production of ionising flux, feedback from wind momentum, star formation history, and galaxy evolution.

Over the past decade, considerable effort has gone into developing new theoretical mass-loss rate recipes based on hydrodynamic wind calculations (Krtićka & Kubát 2017; Gormaz-Matamala et al. 2019; Björklund et al. 2021), with the aim of updating stellar evolutionary models of massive stars. The mass-loss rates (denoted dM/dt or simply \dot{M}) of these new prescriptions are a factor $\sim 2 - 3$ times lower than the smooth rates given by Vink et al. (2001, hereafter V01), which have been the standard recipe adopted in the majority of stellar evolution codes such as GENEC (e.g., Eggenberger et al. 2008), MESA (e.g., Paxton et al. 2011), or BoOST (e.g., Szécsi et al. 2022). Evolution models adopting lower \dot{M} show that massive stars retain more mass during their main sequence phase, thus being bigger

and more luminous (Gormaz-Matamala et al. 2022b; Björklund et al. 2023). Moreover, stars keep larger rotational velocities for a more extended time because they lose less angular momentum (Gormaz-Matamala et al. 2023, 2024), also altering the chemical enrichment at the stellar surface due to rotational mixing. The impact of reduction in \dot{M} goes from different chemical abundances (Gómez-González et al. 2025; Liu et al. 2025), to larger final masses prior to the core-collapse (Gormaz-Matamala et al. 2025; Romagnolo et al. 2024; Kruckow et al. 2024; Costa et al. 2025). Even though these changes in the stellar evolution have been applied mostly at the early H-burning stages, they also impact the evolution of the subsequent stages (Josiek et al. 2024), notwithstanding the importance of upgrading mass-loss rate prescriptions for these advanced stages such as red supergiants (Zapartas et al. 2025) or Wolf-Rayet (WR) stars (Sander et al. 2023).

New models for stellar winds and evolution modify the diagnostics for populations of massive stars. A prime example is the central parsec of the Galactic Centre (hereafter GC), with the largest concentration of massive stars known in the Milky Way. Bartko et al. (2009) identified spectroscopically 90 O/WR stars, while von Fellenberg et al. (2022) increased the sample to 195 but including young B stars also. At the same time, this popula-

tion is puzzling because, even though they are evolved, the stars are ‘young’ (aged $\sim 2 - 8$ Myr) but living in a region hostile for star formation (e.g., Ghez et al. 2003; Genzel et al. 2010), given the tidal field of a supermassive black hole, Sgr A*, with a mass $M_{\text{BH}} \approx 4 \times 10^6 M_{\odot}$ (Schödel et al. 2002). Moreover, this population has a very unusual distribution of luminosities (after correcting for extinction), which implies a very top-heavy initial mass function (e.g., Paumard et al. 2006; Nayakshin et al. 2006; Bartko et al. 2010; Lu et al. 2013; von Fellenberg et al. 2022). Therefore, it is worth revising the observational constraints on the ages and initial masses.

The GC also provides the best chance to study a galactic nucleus, including the accretion on to a super-massive black hole, which in this case is closely connected to the massive stars and their winds. The stars are all confined to a fraction of a parsec, so the winds are expected to collide, convert their kinetic energy into thermal, and create a hot plasma from which the black hole accretes (Quataert 2004). Different groups have modelled the gas dynamics in the GC, using the properties of each star, including their orbits and wind characteristics, as initial conditions (e.g., Cuadra et al. 2008, 2015; Ressler et al. 2018, 2020; Calderón et al. 2020b, 2025). These studies conclude that the accretion onto Sgr A* is more complicated and time-variable, and depends on the wind properties. In particular, of the Wolf-Rayet winds at the central parsec, given that they possess much stronger winds than OB-type stars. For the WR winds with terminal velocity $\gtrsim 1000 \text{ km s}^{-1}$, when they collide gas is heated to $\gtrsim 10^7 \text{ K}$ and cooling takes much longer than the dynamical time, leading to a smooth, Bondi-like accretion. Conversely, after the collision of winds with $v_{\infty} \lesssim 1000 \text{ km s}^{-1}$, gas is heated to $\sim 10^6 \text{ K}$ only, and the cooling process is faster, leading to the formation of clumps of mass up to the order of $10^{-5} M_{\odot}$ (Cuadra et al. 2005; Calderón et al. 2016, 2020a), some of which may have been observed (Gillissen et al. 2012, 2025). Since clumps are present, there are episodes of high accretion superimposed on the smooth accretion rate of the hot plasma. If many clumps reach the black hole vicinity, they can coalesce forming a cold disk-like structure around the black hole Sgr A*, making its growth more efficient (Calderón et al. 2020b, 2025). The chemical composition of the winds is also an important factor. WR stars are losing their atmospheric hydrogen, so their winds can have a hydrogen fraction as high as $\approx 50\%$ and as low as zero. Hydrogen significantly influences the cooling of the gas after the winds shock, as Calderón et al. (2025) demonstrated, potentially tipping the balance on whether a disc forms around the black hole. Observationally, studies using different tracers have found evidence for and against the current presence of such a cold disc around Sgr A* (Murchikova et al. 2019; Ciurlo et al. 2021).

While there have been many studies of the dynamics and origin of the young stellar population in the GC (see, e.g., the review by Mapelli & Gualandris 2016), their atmospheric properties have not received that much attention. The properties of the B-type stars at the GC were studied by Habibi et al. (2017), whereas the O and WR stars were analysed by Martins et al. (2007). In the latter, the evolutionary sequence for the different subtypes of WR stars (Ofpe/WN9, WNL, WNC, WC) was analysed with the evolutionary tracks from Meynet & Maeder (2005), where the outflows for the massive OB-type stars are overestimated. Therefore, the calculation of new self-consistent evolutionary tracks, including a new prescription for \dot{M} , is necessary to further our understanding of not only massive stars and their stellar winds, but also their effects over the interstellar medium and the current growth of the Galactic central black hole.

In this paper, we present a new set of evolutionary tracks adopting new mass-loss rate recipes for the initial OB-type and RSG phases. We describe the physics of our evolution models in Sec. 2 and analyse their results in Sec. 3. We compare our predictions with the observed properties of the stars at the GC in Sec. 4, together with provided insights of the chemical composition and lifetimes of the calculated WR phases. Finally, a summary and conclusions are outlined in Sec. 5.

2. Evolution models

To approach the chemical conditions close to the GC, we model the stellar evolution of stars at super-solar metallicity $Z = 0.020$ (being $Z_{\odot} = 0.0142$ from Asplund et al. 2009), rescaling Z as done by Yusof et al. (2022). The metallicity of the Milky Way is not constant but it decreases according to the Galactocentric distance, with $Z = 0.028 \pm 0.004$ near the GC (Hayden et al. 2014). Measurements at the GC itself are not conclusive, but seem to indicate a $\sim 50\%$ suprasolar abundance of alpha elements and a solar iron abundance (see Genzel et al. 2010, for a review). Our selected $Z = 0.020$ is perhaps a simplification; however, it enables us to make a direct comparison with earlier grids of evolution models such as Yusof et al. (2022), which is the grid with the highest metallicity currently in the literature.

2.1. Mass-loss rate prescription

For OB-type stars we use the mass-loss rate recipe from Krtićka et al. (2024, hereafter K24). This recipe comes from models calculated for O-type stars using the METUJE wind modelling code (Krtićka & Kubát 2017, 2018), and shows a close agreement with the mass-loss rate coming from Gormaz-Matamala et al. (2023, hereafter GM23) for main sequence stars. However, the formula from GM23 is valid for O-type stars with $T_{\text{eff}} \geq 30 \text{ kK}$ only, whereas K24’s is valid for OB-type stars with $T_{\text{eff}} > 10 \text{ kK}$, thus covering also the range of B-supergiants (Krtićka et al. 2021). The so-called bi-stability jump (Pauldrach & Puls 1990) is expected to take place within this temperature range, even though its existence has been debated lately. Vink et al. (2001) predict an abrupt increase in mass-loss rate at $T_{\text{eff}} \approx 25 \text{ kK}$ due to the change in the wind ionisation (Vink et al. 1999), whereas Björklund et al. (2023) predict just a decrease in the mass-loss rate with decreasing temperature without jumps. On its side, the mass-loss rate prescription from Krtićka et al. (2024) finds a gradual rise in \dot{M} also due to the change in the Fe ionisation, below 22 kK with a peak at $T_{\text{eff}} \approx 15 \text{ kK}$, thus more in rule with the observational surveys which have found no drastic jumps in the mass-loss rate of OB-supergiants either in Galactic sources (de Burgos et al. 2024) or in the LMC (Verhamme et al. 2024).

It is worth to mention that METUJE models have been calculated in the metallicity range from $0.2 Z_{\odot}$ to $1 Z_{\odot}$, and thus the K24 mass-loss rate recipe used in this work is an extrapolation towards super-solar metallicity. Standard evolution models adopting \dot{M}_{V01} assume a fixed metallicity dependence of $\dot{M} \propto Z^{0.85}$ for OB-type stars; however, new prescriptions demonstrate that such metallicity dependence varies implicitly with the luminosity or the stellar mass (Krtićka & Kubát 2018; Gormaz-Matamala et al. 2023), given that line driving (metallicity dependent) becomes less dominant than electron scattering (metallicity independent) at larger luminosities, something also observed for WNL stars (Gräfener & Hamann 2008). For the purposes of this paper, given that the increase in metallicity is only a $\approx 42\%$ from 0.014 to 0.020 , the extrapolation adopted by us is still within the expected order of magnitude for the weaker winds.

We also update the mass-loss rate recipe for the region of the Hertzsprung-Russell diagram (HRD) below 10 kK. We keep the default formulation from de Jager et al. (1988, hereafter dJ88) for yellow supergiants ($5 < T_{\text{eff}} < 10$ kK, hereafter YSG), but adopt a new recipe for red supergiants ($T_{\text{eff}} < 5$ kK, hereafter RSG). Unlike line-driven winds, the mechanism for the mass loss of RSG is still uncertain, thought to be a product of dust-driven and low surface gravity (van Loon 2025). Consequently, predictions of \dot{M}_{RSG} show discrepancies of various orders of magnitude (Goldman et al. 2017; Yang et al. 2023; Beasor et al. 2023; Decin et al. 2024), as well as a strong dependence on the assumed turbulent velocity (Kee et al. 2021) or grain size for dust-driven simulations (Antoniadis et al. 2024), thus leading into different evolutionary outcomes. Higher \dot{M}_{RSG} , such as Kee et al. (2021) and Yang et al. (2023), predict that the stars will remove their outer envelopes faster resulting in a moderate population of RSG more in agreement with observations¹ (Zapartas et al. 2025). Despite these scattered results, we incorporate the mass-loss rate for red supergiants ($T_{\text{eff}} < 5$ kK) from Yang et al. (2023, hereafter Y23) in our study, as it aligns with the updated Humphreys-Davidson limit for the SMC (Davies et al. 2018) and M31 (McDonald et al. 2022). Study of Yang et al. (2023) is also focused on the SMC, but since \dot{M}_{RSG} is expected to be independent of Z (Antoniadis et al. 2025) the formula can be easily extended for other metallicities. Besides, a higher mass-loss rate prescription for RSG intrinsically incorporates the existence of sporadic gaseous ejections, which can reach $\dot{M} \sim 3 \times 10^{-3} M_{\odot} \text{ yr}^{-1}$ in some extreme cases (Humphreys & Jones 2022).

For WR winds we keep the mass-loss rate recipes from Nugis & Lamers (2000) and Gräfener & Hamann (2008). The reason is that, for the mass range to be studied (M_{zams} from 20 to 60 M_{\odot}) the WR stars are post RSG, with the Ofpe/WN9 spectral type (Crowther et al. 1995a) as an intermediate phase. More recent formulae for \dot{M} of the WR stars have been explored for the cases where the transition between O-type and WR stages is given by the WNh phase (Bestenlehner 2020) or for H-depleted WR stars (Sander & Vink 2020). Even though these new recipes have been included in studies about stellar evolution (Romagnolo et al. 2024), more detailed analyses on the expected lifetimes and chemical composition of the resulting WR stars have been focused only on very massive stars (Gormaz-Matamala et al. 2025).

The formulae described in this Section are given explicitly in Appendix A.

2.2. Additional setup

We calculate our evolution models using the Geneva-evolution-code (Eggenberger et al. 2008, hereafter GENEC). We keep most of the setup for the inner stellar structure from Ekström et al. (2012) and Yusof et al. (2022), such as step-overshooting $\alpha_{\text{ov}} = l/H_p = 0.1$, whereas we employ the Ledoux criterion for the convective boundaries, in agreement with Georgy et al. (2014), Martinet et al. (2023), and Sibony et al. (2023).

For the treatment of stellar rotation, we keep the original setup from Ekström et al. (2012), with the angular momentum transport described by the advective equations from Zahn (1992), Horizontal and vertical shear diffusion coefficients following Zahn (1992) and Maeder (1997) respectively, notwith-

¹ Notice that ‘higher mass-loss rate’ means ‘higher mass-loss rate at the same HRD location’. The total RSG mass loss may change if the stellar track reaches the red region of the HRD at lower luminosities, as we will see later.

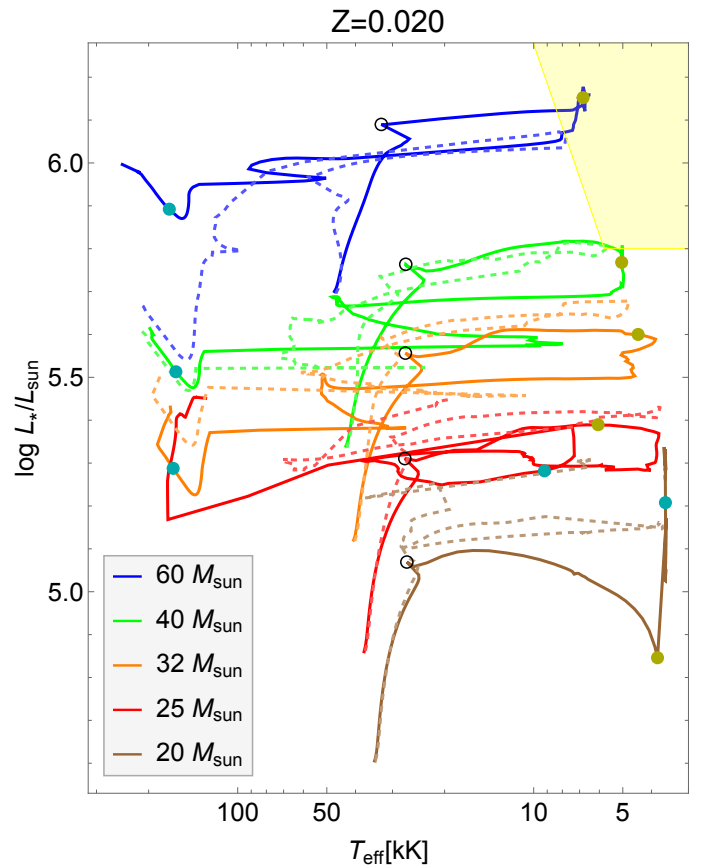


Fig. 1: HR diagram for the new evolution models of this work (solid lines), compared with the old models from Yusof et al. (2022, dashed lines). Empty, dark yellow, and dark cyan circles represent the end of the H-core, the beginning of the He-core, and the end of the He-core burning stages, respectively. The yellow-shaded region corresponds to the zone beyond the Humphreys-Davidson limit, where LBV stars are expected to be found (Humphreys et al. 2016).

standing that different diffusion treatments would lead into diverse results (Nandal et al. 2024). The enhancement of mass-loss due to rotation is given by the correction factor from Maeder & Meynet (2000), which is of the same order as the mass-loss increase described by analytical solutions from the m-CAK theory (Curé 2004; Curé & Rial 2007). The standard initial rotation for the different masses is set to be a 40% of the critical rotational velocity (Ekström et al. 2012; Choi et al. 2016). However, since GENEC incorporate the oblate effects in the stellar structure (Georgy et al. 2011), $v/v_{\text{crit}} \neq \Omega/\Omega_{\text{crit}}$ and thus the initial $v/v_{\text{crit}} = 0.4$ from Yusof et al. (2022) actually is equivalent to $\Omega/\Omega_{\text{crit}} \simeq 0.58$. Hence, we set the initial rotational velocity for our models to be $\Omega/\Omega_{\text{crit}} = 0.4$ ($v/v_{\text{crit}} \simeq 0.28$), matching with other evolution grids such as Choi et al. (2016) and Romagnolo et al. (2024).

3. Results

Figure 1 shows our new evolution tracks across the HR diagram, together with the tracks from Yusof et al. (2022), who used \dot{M}_{v01} for the winds of OB-type stars. The main results from both old and new evolution models are tabulated in Table 1 for the end of the H-core burning, and in Table 2 for the end of He-core and C-core burning stages. The evolution of the stellar rotation during the H-core burning stage, in absolute terms and relative

Table 1: Properties of our selected evolutionary tracks at the end of the H-core burning stage.

M_{zams} [M_{\odot}]		$\log \dot{M}_{\text{zams}}$	$v_{\text{rot,ini}}$	$\langle v_{\text{rot}} \rangle$ [km s^{-1}]	$v_{\text{rot,final}}$	τ_{MS} [Myr]	M_{total} [M_{\odot}]	X_{H}	X_{He}	X_{C}	X_{N}	X_{O}
mass percentage												
60	Y22	-5.60	338.0	120.3	5.2	4.367	34.86	22.39	75.65	0.014	1.152	0.027
60	this work	-6.29	234.0	166.6	3.5	4.027	55.22	49.33	48.69	0.127	0.825	0.336
40	Y22	-6.16	302.0	138.6	5.0	5.600	30.59	44.52	53.51	0.069	0.939	0.202
40	this work	-6.72	215.0	176.2	69.5	5.089	38.24	61.62	36.39	0.213	0.521	0.569
32	Y22	-6.52	297.0	162.6	9.0	6.750	26.90	50.24	47.79	0.112	0.776	0.331
32	this work	-7.02	205.0	173.7	130.0	5.952	31.00	66.68	31.32	0.254	0.365	0.694
25	Y22	-6.99	277.0	191.6	35.4	8.119	23.12	60.49	37.52	0.163	0.543	0.530
25	this work	-7.40	195.0	164.6	160.0	7.208	24.51	68.92	29.07	0.270	0.283	0.765
20	Y22	-7.48	267.0	209.2	133.0	9.602	19.37	67.06	30.93	0.193	0.381	0.676
20	this work	-7.80	185.0	154.9	167.0	9.018	19.76	69.78	28.20	0.272	0.251	0.799

Notes. Values for tracks adopting Vink's formula are taken from Yusof et al. (2022).

Table 2: Properties of our selected evolutionary tracks at the end of the He-core and the C-core burning stages.

M_{zams} [M_{\odot}]	\dot{M} recipe	Age [Myr]	M_{total} [M_{\odot}]	X_{H}	X_{He}	X_{C}	X_{N}	X_{O}	Age [Myr]	M_{total} [M_{\odot}]	X_{H}	X_{He}	X_{C}	X_{N}	X_{O}
mass percentage															
60	Y22	4.768	12.89	0	26.78	50.31	0	20.33	4.769	12.88	0	26.65	50.32	0	20.44
60	this work	4.394	21.39	0	24.00	46.11	0.001	27.24	4.398	21.30	0	23.62	46.02	0.001	27.71
40	Y22	6.037	11.65	0	27.16	51.08	0	19.17	6.039	11.63	0	27.07	51.09	0	19.25
40	this work	5.540	11.86	0	24.82	48.94	0.026	23.61	5.546	11.78	0	24.31	48.95	0.024	24.11
32	Y22	7.271	9.83	0	25.82	50.48	0.033	21.07	7.274	9.80	0	25.51	50.55	0.030	21.32
32	this work	6.493	8.49	0	27.03	49.02	0.106	21.26	6.501	8.41	0	26.31	49.12	0.098	21.88
25	Y22	8.736	9.16	0	95.71	0.888	2.336	0.166	8.739	9.08	0	95.63	1.047	2.244	0.175
25	this work	7.940	8.86	0.003	71.91	9.973	7.771	8.907	7.950	8.68	0	38.42	24.44	0.502	33.49
20	Y22	10.425	7.35	31.54	66.49	0.009	1.014	0.198	10.435	7.27	21.95	76.08	0.011	1.100	0.101
20	this work	9.799	12.26	60.12	37.88	0.160	0.555	0.602	9.812	11.81	59.96	38.04	0.157	0.560	0.599

Notes. Values for tracks adopting Vink's formula are taken from Yusof et al. (2022).

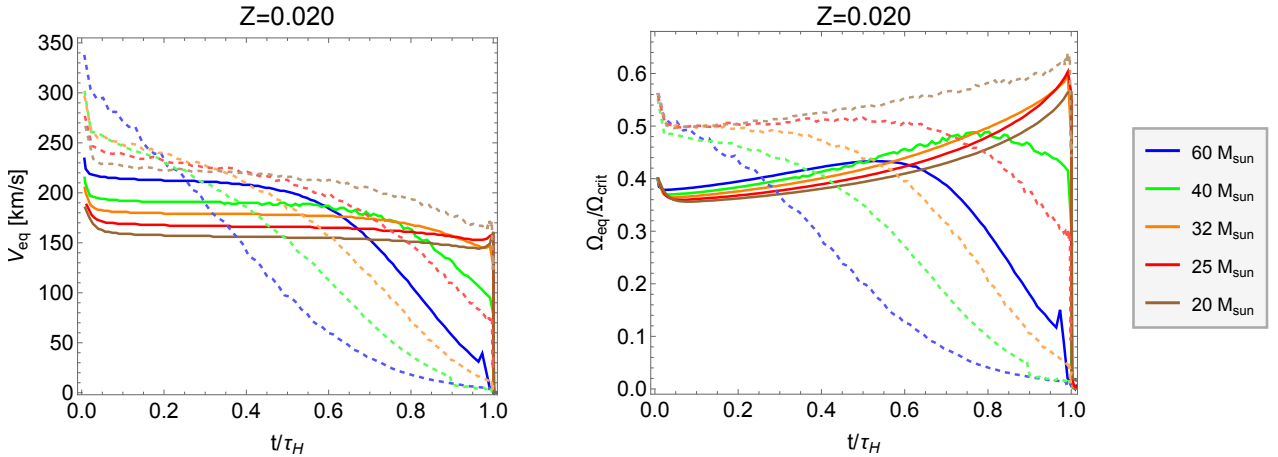


Fig. 2: Evolution of rotational velocity expressed as absolute magnitude v_{rot} (left panel) and angular velocity as fraction of the critical velocity $\Omega/\Omega_{\text{crit}}$ (right panel), as a function of the H-core burning lifetime τ_{H} . Solid and dashed lines represent new and old models respectively, same as for Fig. 1.

to the critical rotational velocity, is shown in Fig. 2. The mass of the convective cores as fractions of the stellar masses during the H-core, H-shell, and He-core burning stages, are shown in Fig. 3.

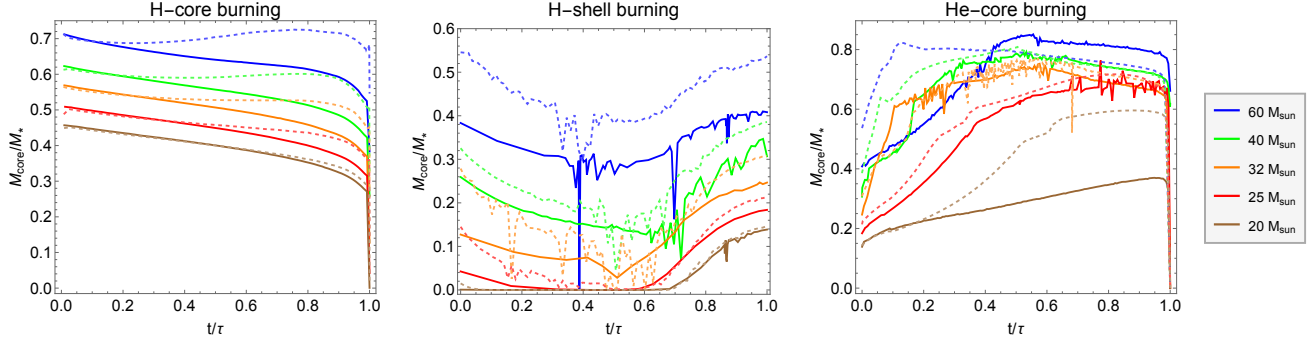


Fig. 3: Evolution of the convective cores, as fractions of the total stellar mass, for our models during the H-core, H-shell and He-core stages. Solid and dashed lines represent new and old models respectively, same as for Fig. 1.

3.1. Evolution during the main sequence stage

In line with Krtićka & Kubát (2018) and Gormaz-Matamala et al. (2022a), we see that the mass-loss rates from K24 are ~ 3 times (for $M_{\text{zams}} = 20 M_{\odot}$) to ~ 5 times (for $M_{\text{zams}} = 60 M_{\odot}$) weaker than V01. For main sequence stars, as also observed for low metallicity environments (Gormaz-Matamala et al. 2024), a reduction of mass loss also implies a reduction in the loss of angular momentum, resulting in a nearly constant rotational velocity during the first half of the main sequence prior to the final decrease in velocity, contrary to the abrupt initial deceleration predicted by older models shown in Fig. 2. This is the reason why, despite starting our models with lower $v_{\text{rot,ini}}$ in comparison with Yusof et al. (2022), our models have a larger average rotational velocity (v_{rot}) for the most massive cases.

The combination of both conditions, lower initial \dot{M} and lower initial v_{rot} , produces a less homogeneous inner structure. Reduced mass loss makes stars to retain more of their outer envelopes, whereas lower rotation produces less efficient internal mixing. Thus, the models show redder tracks through the main sequence as seen in Fig. 1 (and thus a larger radial expansion) as a consequence of the less homogeneous chemical evolution (Maeder 1987; Meynet et al. 2013), thus ending the main sequence with cooler stellar temperatures. This scenario was also observed when only isolated changes in \dot{M} formula were implemented (Gormaz-Matamala et al. 2023), demonstrating that the lower mass loss is far more influential than the reduced rotation. A less efficient mixing also means a lower lifetime for the H-core burning process, because the core is less likely to be refilled with hydrogen from the upper layers, and also a more moderate chemical enrichment in the stellar surface, where the new models exhibit larger fractions of hydrogen in comparison with the models from Yusof et al. (2022). Similarly, the CNO abundances at the stellar surface are affected. The H-burning CNO bi-cycle causes nitrogen to accumulate in the core at the expense of carbon and oxygen. These changes are subsequently transferred to the surface through rotational mixing and the removal of outer envelopes, as outlined by Przybilla et al. (2010) and Maeder et al. (2014). Consequently, the new models (with reduced mass loss and mixing) exhibit smaller mass fractions of nitrogen at the end of the main sequence, while larger mass fractions of carbon and oxygen are observed. The less homogeneous structure is also expressed in lower fractions for the convective core mass (Fig. 3), because of the larger total mass.

The differences between the new evolution models and the ones from Yusof et al. (2022) are more prominent as we escalate in the initial mass. For $M_{\text{zams}} = 32 M_{\odot}$ and above, the reduction of stellar mass at the end of the H-core burning is more

Table 3: Time interval and mass lost during the crossing of the Hertzsprung gap, according to our models.

M_{zams} [M_{\odot}]		Δt [kyr]	ΔM_* [M_{\odot}]
60	Y22	3.872	0.166
60	this work	2.642	0.008
40	Y22	5.571	0.546
40	this work	3.960	0.003
32	Y22	6.491	0.256
32	this work	6.063	0.004
25	Y22	10.415	0.166
25	this work	8.976	0.0019
20	Y22	16.696	0.090
20	this work	12.947	0.0015

moderate for the new models. Adopting updated mass-loss rate prescriptions, our model with an initial mass of $M_{\text{zams}} = 32 M_{\odot}$ loses only $1 M_{\odot}$ during the main sequence, compared to $\approx 5 M_{\odot}$ predicted by the old model. Similarly, our model with $M_{\text{zams}} = 60$ loses only $\approx 5 M_{\odot}$ during the main sequence, compared to $\approx 25 M_{\odot}$ predicted by the old model. Hence, while Yusof et al. (2022) predict stars to lose up to half of their initial masses during the H-core burning, our new models predict a loss of only $\sim 8\%$ at the most². Such significant differences suggest substantial changes in subsequent evolutionary stages, even if other wind recipes remained unchanged, as will be discussed further.

3.2. Evolution post main sequence stage

3.2.1. H-shell burning stage

After the hydrogen depletion at the core, the H-shell burning stage begins, contracting the (now) He-core and expanding the outer layers (Groh et al. 2014). For this reason, all of our models quickly expand radially crossing the HR diagram horizontally at almost constant luminosity, the so-called Hertzsprung gap (HG, Hurley et al. 2000), reaching temperatures below 10 kK at the

² This comparison is done, of course, considering the maximum mass $M_{\text{zams}} = 60 M_{\odot}$ in our analysis. More massive cases would develop WR winds during the main sequence, either from extreme removal of their outer envelopes or due to the proximity to the Eddington limit (see Gormaz-Matamala et al. 2025), so we do not include them here.

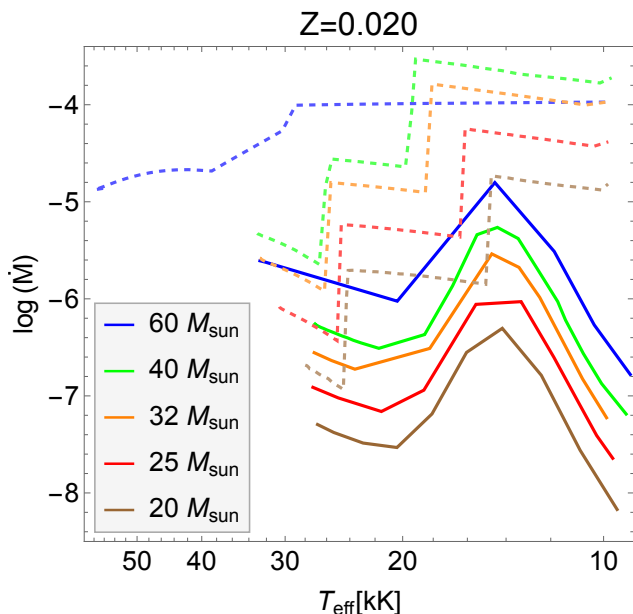


Fig. 4: Mass-loss rates after the H-depletion, as a function of the effective temperature, for the evolution tracks from Yusof et al. (2022, dashed lines) and the tracks from this work (solid lines). Solid and dashed lines represent new and old models respectively, same as for Fig. 1.

end of the HG. Crossing $T_{\text{eff}} = 10$ kK implies a change in the mass-loss rate recipe from K24 to de Jager et al. (1988), but the rapid expansion just culminates when the He-core reaches temperatures high enough to start the He-burning process (He-ignition), which occurs at the red region of the HR diagram as seen in Fig. 1.

During this expansion the stars experience a peak in the mass-loss rate at $T_{\text{eff}} \sim 15$ kK according to the K24 formula (A.1), and thus the removed mass is lower than the predicted by previous models due to the bi-stability jump. This is explicitly evidenced in Fig. 4, where not only the overall mass loss is lower for new models, but also the jumps predicted by V01 do not longer exist. Differences in the mass loss crossing the HG can reach up to two orders of magnitude, with the new values for $\dot{M} \sim 10^{-7} - 10^{-6} M_{\odot} \text{ yr}^{-1}$ more in agreement with the m-CAK δ -slow wind solutions for the regime of B-supergiants (Araya et al. 2021; Venero et al. 2024). Besides, the radial expansion across the Hertzsprung gap is faster because of the choice of the Ledoux criterion instead of Schwarzschild's: the (molecular weight) μ -gradient at the border of the core prevents convection in the deep layers, weakening the support of the star that hence crosses rapidly the Hertzsprung gap (Sibony et al. 2023). In the case of the $20 M_{\odot}$, this happens too quickly (relatively to the Kelvin-Helmholtz timescale) for the thermal equilibrium to happen, so its radiation goes into expanding the envelope, which explains the drop in luminosity. Table 3 shows the time required for the star to evolve from the end of the main sequence to the end of the HG: the lower mass loss combined with the shorter cross means that new models lose an amount of mass almost negligible when they cross the HG. Consequently, the envelope removal is almost negligible, so we can assume that the chemical composition of the stars is almost the same as the one tabulated for the end of the H-core burning.

3.2.2. He-core and C-core burning stages

The higher \dot{M} from Yang et al. (2023) makes our model of $M_{\text{zams}} = 40 M_{\odot}$ to experience a strong mass removal of the order of $\log \dot{M}_{\text{Y23}} \approx -1.8$ when it crosses the threshold of $T_{\text{eff}} = 5$ kK, with a subsequent drift back to $T_{\text{eff}} > 5$ kK, thus entering in a loop between both wind regimes dJ88 and Y23. This is a numerical artefact, but it can be physically interpreted as our $40 M_{\odot}$ being subject to strong and variable outflows around ~ 5 kK, which prevents the star from becoming a RSG. Hence, the higher \dot{M} from Yang et al. (2023) for $T_{\text{eff}} < 5$ kK helps to preserve the upper Humphreys-Davidson limit (Humphreys et al. 2016) on $\log(L/L_{\odot}) \approx 5.5$ from Davies et al. (2018) and McDonald et al. (2022), besides also reducing the total time spent in the RSG phase (Zapartas et al. 2025). Indeed, the higher \dot{M}_{Y23} produces the biggest mass removal during the entire evolution of our stars (as shown by the black lines in Fig. 5). Additionally, the more efficient peeling-off effect during the RSG phase reduces the minimum initial mass required for a star to become a Wolf-Rayet. RSGs evolve blueward in the HR diagram when the mass of their convective cores reaches 60% of the total mass (Meynet et al. 2015). Even though new models start their He-ignition with lower M_{core}/M_{*} ratios (left panel of Fig. 3), the extra removal of outer envelopes compensates this condition and thus all stars with $M_{\text{zams}} \geq 25 M_{\odot}$ will continue evolving into WR stars. The exception is our $20 M_{\odot}$ model, which reaches the RSG phase with a luminosity $\log(L/L_{\odot}) < 5.0$ (in contrast with the ≈ 5.2 from Yusof et al. 2022), thus resulting in a lower \dot{M}_{RSG} and in a poorer chemical enrichment at the stellar surface, at the end of the He-core and C-core burning stages.

The rest of our models continue evolving towards the Wolf-Rayet phases. For the stars with 25 and $32 M_{\odot}$, new models predict lower final masses at the end of their lives (8.68 and $8.41 M_{\odot}$ respectively), which are even lower than the final mass predicted for $M_{\text{zams}} = 20 M_{\odot}$. After the RSG phase, which corresponds to the abrupt drops in mass fraction and hydrogen, new models with 25 and $32 M_{\odot}$ end up with lower masses (compared with old models), whereas the opposite happens for models with 40 and $60 M_{\odot}$. And yet all models leave the RSG phase with larger H/He ratio, as a consequence of the lower mixing during the earlier evolutionary stages. According to Nugis & Lamers (2000) and Gräfener & Hamann (2008) recipes, \dot{M}_{WR} is more moderate for stars with larger H/He, and thus WR stars will initially lose less mass and envelope. However, this initially lower \dot{M}_{WR} creates a larger inhomogeneity in the inner stellar structure, making evolution tracks to move more redwards during their WR lifetime, as noted in the HR diagram, and thus experiencing inflation episodes due to supra-Eddington layers (Ekström et al. 2012). As a result, the envelope removal of these WR stars is speeded up as they continue evolving. The case of $M_{\text{zams}} = 25 M_{\odot}$ is particularly noteworthy, because it makes the new track to continue evolving towards the WC phase (where carbon and oxygen become $\sim 70\%$ of the surface composition), in contrast with the old model which predicts a final state as an almost pure He-star ($\approx 96\%$ of its surface composition).

For the most massive cases, this effect is less relevant. The model with $32 M_{\odot}$ ends up with less mass but with a chemical composition at the end of the C-core burning stage comparable to the one predicted by Yusof et al. (2022). For $40 M_{\odot}$, \dot{M}_{Y23} prevented the model from becoming an RSG star, but still resulted in a significant mass removal, compensating for initial deviations during the OB-type mass-loss phase, and explaining why the final mass and final chemical compositions are quite similar for both old and new models. For $60 M_{\odot}$, the deviations during the

main sequence were substantial enough to persist through subsequent stages, particularly since it never became an RSG, resulting in a final mass predicted by the new model ($21.3 M_{\odot}$) that is approximately 65% higher than that of the old model.

4. Stellar properties at the Galactic Centre

We now proceed to evaluate the current evolutionary status of the massive stars at the Galactic Centre, according to our new evolution tracks. We are particularly interested in the chemical surface abundance of these stars, given their influence on the accretion on to the central super-massive black hole (e.g., Calderón et al. 2025). Despite the known kinematics of hundreds of massive stars in the central parsec of the Milky Way (von Fellenberg et al. 2022), the only stars with measured stellar properties are the sample of WR stars from Martins et al. (2007) and the so-called ‘S-stars’ from Habibi et al. (2017). These S-stars, however, are spectroscopically B-dwarfs (i.e., early main sequence stars without any wind) with initial masses between $\sim 7-15 M_{\odot}$, whose evolutionary status is barely affected by updated wind mass-loss rate prescriptions. Therefore, our observational analysis is focused on the sample of WR stars.

4.1. Theoretical predictions for observed WR stars

For the case of WR stars at the Galactic Centre, the known sample includes spectral types Ofpe/WN9, WN (subtypes 5 to 8), WN/C, and WC (subtypes 8 and 9). Their determined temperatures, luminosities, and abundances are given by Martins et al. (2007, see their Table 2).

4.1.1. Ofpe/WN9 and WN stars

The left panel of Fig. 6 shows the hydrogen fraction as a function of luminosity, starting from the He-ignition, for both old and new evolution tracks. This figure is analogous to Fig. 21 by Martins et al. (2007), where the used tracks were from Meynet & Maeder (2005). From here, it was deduced that Ofpe/WN9 are immediate precursors of WR stars. However, because the post-MS stellar evolution for stars in the range of 25 to $60 M_{\odot}$ is at almost constant luminosity, the plane $X_{\text{surf}} - L_{*}$ is not enough to provide insights on the evolution status of these stars. For that reason, we add a second panel on the right showing the hydrogen mass fraction but as a function of the stellar temperature (the radius rescaling is taken from Meynet & Maeder 2005), also from the start of the He-core burning. Given that all our models start their He-ignition with $T_{\text{eff}} < 10$ kK (Fig. 1), they begin being YSG/RSG stars losing surface hydrogen at almost constant temperature before continuing evolving bluewards post-YSG/RSG. New models predict post-YSG/RSG evolution to be H-richer than their counterparts predicted by Yusof et al. (2022), making them also redder. Hence, we can see that the hydrogen mass fractions predicted by our evolution models, for both post-RSG and post-YSG phases, do a good match with the high X_{H} exhibited by these Ofpe/WN9 stars. This, notwithstanding the possibility of some of these Ofpe/WN9 being in a quiescent LBV state (Crowther et al. 1995a), in particular the stars with the largest hydrogen content.

Certainly all the evidence supports that Ofpe/WN9 are precursors of late-type WN stars, but this does not necessarily mean that WN8 will be the immediate stage after. Figure 6 also shows that, with the exception of the $60 M_{\odot}$ model, the new tracks for post Ofpe/WN9 phase start decreasing their temperatures as the

surface hydrogen goes below $\sim 20\%$. If we consider $X_{\text{H}} = 0.2$ to be the threshold between Ofpe/WN9 and WNL stars (a reasonable assumption, given the observed abundances of the Martins et al. 2007, sample), we can suggest that the temporal sequence for the initial mass range $\sim 25 - 40 M_{\odot}$ is not descendent from WN8 to earlier WNL (subtypes 7 and 6) but the opposite (Ofpe/WN9 \rightarrow WN6 \rightarrow WN7 \rightarrow WN8 \rightarrow ...), or even non monotonic. Naturally this statement is not conclusive given that the actual distinctions between the WN subtypes are not based on evolutionary properties but on the properties of the He and N lines (Smith et al. 1996; Crowther 2007). However, the surface nitrogen abundance actually increases from the beginning of the WR phase (Fig. 5) whereas observed WN8 and WN8/WC9 stars contain more nitrogen than their earlier siblings WN 5/6 and WN 7 (Martins et al. 2007, Table 2), thus supporting our assessment. This means, WN8 stars at the GC are closer to the other subtypes WN5-7 rather than to Ofpe/WN9, this is the reason why they should be included in the same WNL subcategory for posteriori wind colliding models (compare with the input of sub-groups of WR stars adopted by Calderón et al. 2025).

4.1.2. WN/C and WC stars

WN/C stars are WR stars which exhibit an equilibrium between nitrogen and carbon at their surfaces (C/N ratio of the order of 1). This spectral type is expected to be found for stars born with masses between ~ 30 and $60 M_{\odot}$, massive enough to show He-burning nuclear waste (carbon) before their core collapse, but not so massive to not be quickly depleted of all its surface hydrogen before becoming WC (Meynet & Maeder 2003). When the WR phase starts, the stellar surface is very C-poor because the CNO cycle converts carbon into nitrogen, but it becomes C-rich as the products of the He-burning (carbon and oxygen) start appearing in the outer envelopes. Nitrogen abundance also increases during the WR phase, as shown by Fig. 5, but at a smaller rate than carbon, reason why this ratio C/N grows up.

Such evolutionary diagnostics are based on solar metallicity (assuming $Z_{\odot} = 0.02$), but still fits quite well with our set of new evolution models. Figure 7 shows the evolution of the C/He ratio post-YSG/RSG as a function of the stellar luminosity (left panel) and temperature (right panel), for both new and old tracks. The surface carbon abundance increases as the WR stars slightly decrease their temperatures, with the WN/C stars from Martins et al. (2007) located prior to the end of this redwards drift. As for Martins’ WC stars, the C/He ratio coincides with the rapid jump in temperature in the new models which overcomes with the removal of the last traces of hydrogen (i.e., with the end of any WN signature). Still, this behaviour of C/He vs T_{eff} is found for both old and new evolution tracks. The differences come when we analyse the C/He ratio against the luminosity. Given that our $25 M_{\odot}$ model continues evolving towards the WC phase, it matches better the less bright WN/C and WC stars analysed by Martins et al. (2007), without the need of invoking binary evolution.

If the latest traces of hydrogen are still present in the outer envelope of our structure models, the calculated opacity for this outer envelope becomes uncertain and subsequently the radius can be numerically inflated, with the respective drop in the temperature. This opacity effect is an inherent condition produced by the mismatch between (hydrostatic) evolution models and (expanding) atmospheric models. Even though ‘deep’ expanding atmospheric models can correct the expected temperatures predicted in GENEC models subject to envelope inflation, it requires a considerable computational effort and it has been implemented only for the main sequence stage of very massive

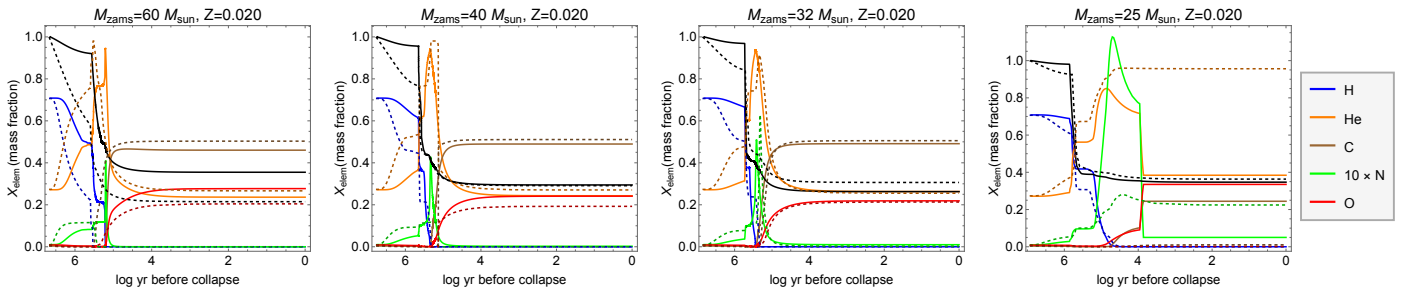


Fig. 5: Evolution of the surface abundances for hydrogen, helium, carbon, nitrogen, and oxygen, for the models reaching the WR phase. Black lines represent the total mass fraction, M_*/M_{zams} . The nitrogen abundance is multiplied by 10, for illustrative purposes.

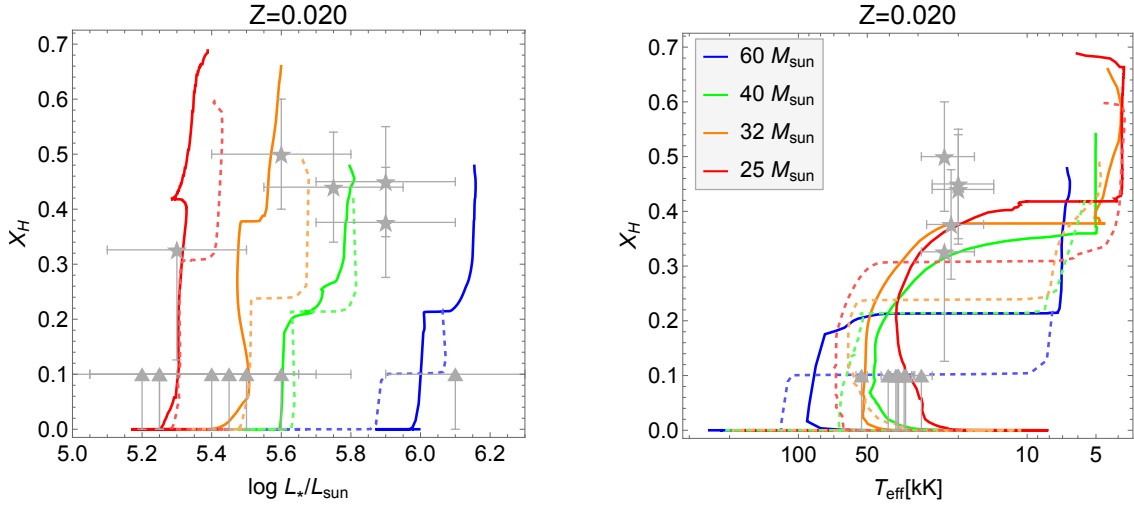


Fig. 6: Left panel: hydrogen mass fraction at the stellar surface as a function of the stellar luminosity, from the H-core ignition to the C-core depletion. Right panel: hydrogen mass fraction at the stellar surface as a function of the stellar temperature, from He-ignition to the C-core depletion. Grey stars and triangles represent the observational values calculated by Martins et al. (2007), for Ofpe/WN9 and WN stars respectively. Solid and dashed lines represent new and old models respectively, same as for Fig. 1.

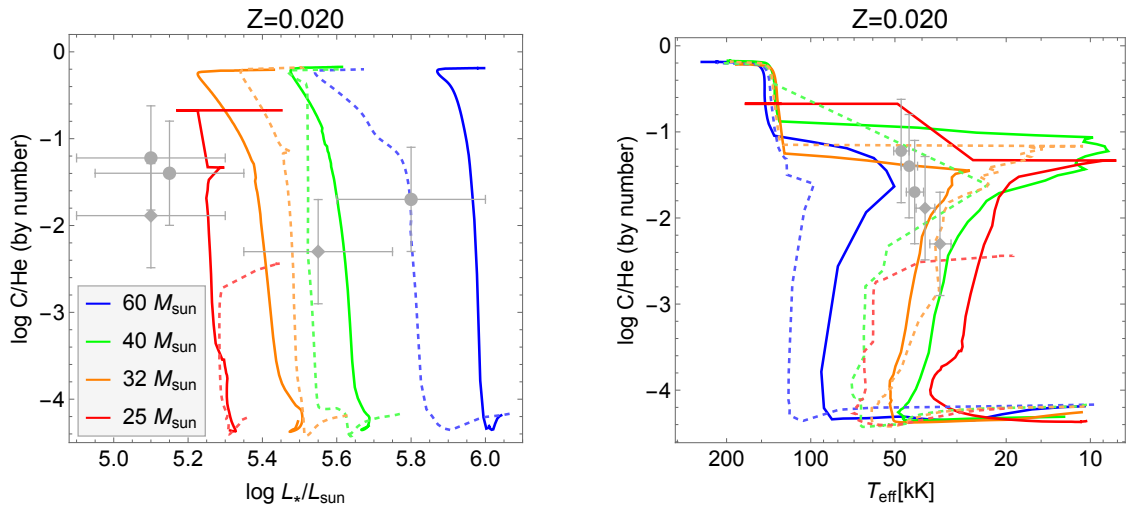


Fig. 7: Left panel: carbon-to-helium ratio (by number) at the stellar surface as a function of the stellar luminosity, from post YSG/RSG phase to the C-depletion. Right panel: carbon-to-helium ratio (by number) at the stellar surface as a function of the stellar temperature, from post YSG/RSG phase to the C-depletion. Grey diamonds and circles represent the observational values calculated by Martins et al. (2007), for WN/C and WC stars respectively. Solid and dashed lines represent new and old models respectively, same as for Fig. 1.

stars (Josiek et al. 2025). However, this opacity effect represents a minimal fraction of the WR lifetime, and does not interfere with the chemical composition nor temperatures measured for the WN/C and WC stars in the sample. Therefore, despite this

issue and the associated error bars in the infrared spectra, new evolution tracks at super solar metallicity can adequately reproduce the observational diagnostics for the massive stars of the Galactic Centre.

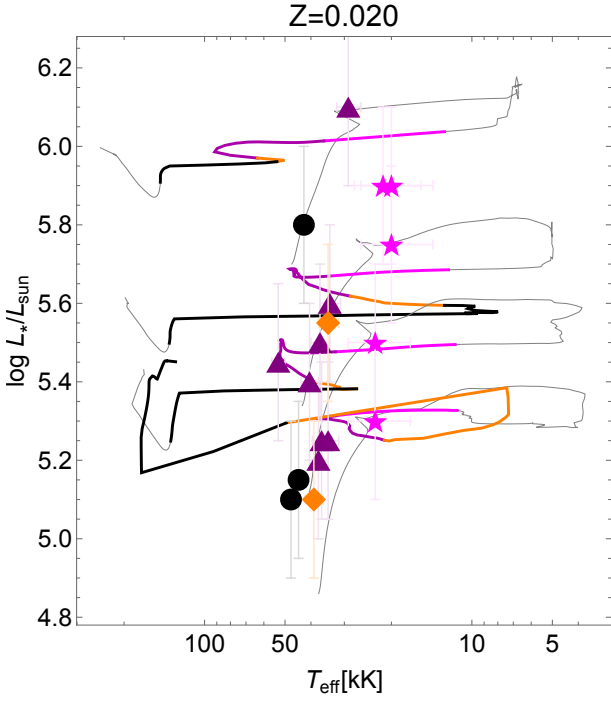


Fig. 8: HR diagram showing the position of the spectroscopic phases Ofpe/WN9 (magenta), WN (purple), WN/C (orange) and WC (black). Observed stars from Martins et al. (2007) are shown, with the same symbols as Fig. 6 and Fig. 7.

4.2. Evolutionary phases

Following Martinet et al. (2023), we proceed to define the WR subtypes as evolutionary stages. Since we cannot use spectroscopic criteria for these categories (because we are not providing synthetic spectra), we use as criteria some abundances and the temperature calculated by our models. Hence

- Ofpe/WN9: WR star with $X_H \geq 0.2$ and $T_* \leq 30$ kK.
- eWNL: WR star with $X_H \geq 10^{-5}$.
- eWNE: WR star and $X_H < 10^{-5}$ and $X_N > X_C$.
- WN/C: WR star with $-0.5 < \log(X_C/X_N) < 0.5$.
- WC: WR star with $\log T_* < 5.20$ and $(X_C + X_O)/X_{He} < 1.6$.

The threshold for Ofpe/WN9 stars come from the analysis of Sec. 4.1.1 and from the parameters calculated by Crowther et al. (1995a). The boundary $X_H = 10^{-5}$ for eWNL and eWNE (where the ‘e’ stands for ‘evolutionary’, following Foellmi et al. 2003) comes from Georgy et al. (2012). The boundaries for the WN/C phase are in rule with the C/N values reported by Crowther et al. (1995b). The separation between WC and WO comes from the C, O, and He abundances measured by Aadland et al. (2022).

We highlight the segment of each one of the Wolf-Rayet phases (Ofpe/WN9, WNL, WN/C and WC) across the HR diagram in Fig. 8, together with the GC stars from Martins et al. (2007). In general we notice a consistency between observed and evolutionary spectral type, with some minor discrepancies due to the lack of unified criteria. For example, our C/N abundances for the WN/C phase differ from the boundaries used by Georgy et al. (2012), where WN/C stars are additionally expected to be H-poor. In our case, given the moderate chemical evolution consequence of lower winds, we still find traces of hydrogen at the surface of WN/C stars. This is observed in Fig. 9, where new evolution models predict stars to become carbon-richer prior to the total depletion of hydrogen from the stellar surface. In contrast, old models predict stars with $X_{\text{surf}} \leq 10^{-5}$ and $X_N > X_C$,

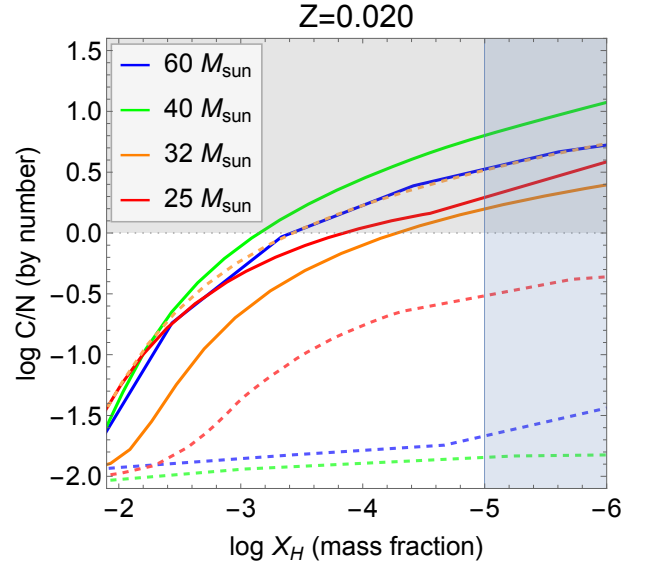


Fig. 9: Evolution of the C/N ratio in evolution models, as the stars are losing their last 1% of hydrogen in the outer layer. Blue-shaded region represents $X_H \leq 10^{-5}$ and $X_C \geq X_N$, whereas grey-shaded region $X_H \geq 10^{-5}$ and $X_C \leq X_N$. Solid and dashed lines represent new and old models respectively, same as for Fig. 1.

thus being in the category of eWNE stars. Thus, all our evolution models predict that (H-rich) WNL stars evolve into WN/C without passing through eWNE phase. This is consistent with the lack of early type WN stars in the sample of Martins et al. (2007), where the earliest WN star is 16SE2 with spectroscopic subtype WN5/6. Besides, as mentioned in Sec. 4.1.1, the low nitrogen content of 16SE2 suggests that this WN5/6 might be located before the WN7-8 stars in the evolutionary sequence, strengthening the idea of the WNL phase being the direct precursor of WN/C for the mass and metallicity range analysed in this work. Again, the aforementioned by-pass to the eWNE phase is based only on the abundance criteria coming from the evolution models instead of from spectroscopic features, so it cannot be taken as a full absence of WNE stars in the GC.

Now we proceed to calculate the surface abundances for hydrogen, helium, carbon, nitrogen, and oxygen, for our evolution models during Ofpe/WN9, WNL, WN/C, and WC phases. Given that the individual surface abundances are still changing within the same spectral subtypes, we calculate the time-averaged abundances, defined as

$$\langle X_{\text{elem}} \rangle = \frac{1}{\Delta\tau_{\text{phase}}} \int_{t_i}^{t_f} X_{\text{elem}}(t) dt, \quad (1)$$

where $\Delta\tau_{\text{phase}} = t_f - t_i$ (t_f – final time, t_i – initial time) is the lifetime of the respective subtype, and the corresponding uncertainties as the standard deviations,

$$\sigma(X_{\text{elem}}) = \sqrt{\frac{1}{\Delta\tau_{\text{phase}}} \int_{t_i}^{t_f} [X_{\text{elem}}(t) - \langle X_{\text{elem}} \rangle]^2 dt}. \quad (2)$$

Results for the WR phases are shown in Table 4, together with the lifetime of the spectroscopic phases and the average mass-loss rate (calculated as $\Delta M_{*,\text{lost}}/\Delta\tau_{\text{phase}}$). WR stars are less chemically evolved at their surface for lower initial masses. For Ofpe/WN9 phase, the model with $M_{\text{zams}} = 25 M_{\odot}$ presents the largest hydrogen mass fraction, given that it experienced less mass removal than their counterparts, which was also seen in

the right panel of Fig. 6. It also has the longest lifetime given that the mass loss during this Ofpe/WN9 is the most reduced. For the WN phase, the abundances have a larger standard deviation as a consequence of the quick changes in the chemical composition. For WN/C and WC stars, the abundances are mostly of the same orders of magnitude, with the notable exception of $M_{\text{zams}} = 25 M_{\odot}$, which is the only model reaching the end of the He-core burning stage in the WN/C phase and then it becomes a WC star only at the very end prior to the end of C-core burning.

These tabulated abundances represent an important upgrade for the modelling of the Galactic centre environment around Sgr A*. Recent works have adopted the chemical composition from a selection of observed WR stars, first compiled by Russell et al. (2017) and used in that study and by Wang et al. (2020); Balakrishnan et al. (2024) to produce synthetic X-ray spectra from hydrodynamical simulations, and more recently by Calderón et al. (2025) and Labaj et al. (2025) as a simulation ingredient. Those stars were classified as either WC8-9, WN5-7, and WN8-9 and Ofpe/WN9 stars, with the last two subtypes treated as a single category, with $X_{\text{H}} = 11.5$ and $X_{\text{He}} = 82.5$. However, our evolution models suggest that WN8 may not be the direct descendent of Ofpe/WN9, and for that reason we consider they should not be combined. Indeed, Ofpe/WN9 stars are expected to have higher hydrogen abundances, in line with the spectral diagnostics performed by Martins et al. (2007). Likewise, evolutionary WN5-8 stars as a whole category are now expected to contain a higher fraction of hydrogen due to their previous evolutionary stages, although with a large standard deviations. On the other side, the average abundances for WC are more in agreement with the data tabulated by Russell et al. (2017), with the exception of our $25 M_{\odot}$ model for the reasons given in the previous paragraph.

All in all, our new abundances lie in between those used previously in the literature for hydrodynamical simulations of the Galactic centre WR winds, namely either Solar with three times enhanced metallicity (e.g., Calderón et al. 2020b), or the Russell et al. (2017) tabulated abundances (Calderón et al. 2025). The former resulted in a higher rate of radiative cooling after the wind shock collisions, and the subsequent formation of clumps and even a cold disc that increased the accretion on to Sgr A*, while in the latter those effects were suppressed. Updated hydrodynamical models should be developed using the abundances obtained in this work, for which not only the spectral type of the stars can be used, but also estimates of their masses when available.

5. Summary and conclusions

We show a set of evolutionary tracks using the Geneva-evolution-code (GENEC), for stars with initial masses from 20 to $60 M_{\odot}$, with new mass-loss rate recipes for the winds of OB-type stars (Krtićka et al. 2024) and RSGs (Yang et al. 2023). Because of the lower \dot{M} during the main sequence stage and the Hertzsprung gap, stars retain more than $\approx 92\%$ of their initial masses prior to the stronger dust-driven mass loss at the red part of the HRD, where the star finally loses most of its envelopes.

These changes in the mass-loss history lead into Wolf-Rayet stars with a less evolved chemical evolution (and subsequently 'cooler') in comparison with previous models (Yusof et al. 2022). Post Ofpe/WN9 spectral phase, stars stay as late-type WN to become WN/C, by-passing the early-type WN spectral phase. This scenario agrees with the observed population of WR in the GC (Martins et al. 2007), where the late-type clearly dominates for all WN, WN/C and WC subtypes. Based on this scenario,

we tabulate the respective mean surface abundances and lifetimes of each one of the WR spectroscopic phases, to provide a more robust framework for the study of the colliding winds from the population of WR stars around the supermassive black-hole Sgr A* at the centre of the Milky Way (Calderón et al. 2025).

The results presented in this work represent the state-of-the-art in terms of stellar wind theory, stellar evolution at high metallicity environments, and observations of the Galactic Centre. Considering that $Z = 0.020$ represents a lower threshold for the probable metallicity of the centre of the Milky Way, further studies need to be performed with a wind theory capable of providing adequate values of mass loss at higher Z . Likewise, new spectroscopic measurements are needed for the population of WR stars in the GC in order to decrease the uncertainties in the currently known abundances as well as on their actual wind properties (\dot{M} and v_{∞}). Nevertheless, the new evolutionary tracks introduced in this work as well as the surface abundances predicted for WR stages represent an important upgrade in our understanding on the physical conditions in the Galactic Centre, and they will be the initial starting point for future population synthesis studies for colliding winds.

Acknowledgements. We acknowledge useful discussions with Diego Calderón, Chris Russell, Wasif Shaqil, and Sebastiano von Fellenberg. ACGM thanks the support from project 10108195 MERIT (MSCA-COFUND Horizon Europe). ACGM and JC acknowledge the support from the Max Planck Society through a "Partner Group" grant. JC acknowledges financial support from ANID – FONDECYT Regular 1251444, and Millennium Science Initiative Program NCN2023_002. BK and JK acknowledge support from the Grant Agency of the Czech Republic (GAČR 25-15910S). SE acknowledges support from the Swiss National Science Foundation (SNSF), grant number 212143. The Astronomical Institute of the Czech Academy of Sciences in Ondřejov is supported by the project RVO: 67985815.

References

- Aadland, E., Massey, P., Hillier, D. J., et al. 2022, *ApJ*, 931, 157
 Antoniadis, K., Bonanos, A. Z., de Wit, S., et al. 2024, *A&A*, 686, A88
 Antoniadis, K., Zapartas, E., Bonanos, A. Z., et al. 2025, *A&A*, 702, A178
 Araya, I., Christen, A., Curé, M., et al. 2021, *MNRAS*, 504, 2550
 Asplund, M., Grevesse, N., Sauval, A. J., & Scott, P. 2009, *ARA&A*, 47, 481
 Balakrishnan, M., Russell, C. M. P., Corrales, L., et al. 2024, *ApJ*, 974, 99
 Bartko, H., Martins, F., Fritz, T. K., et al. 2009, *ApJ*, 697, 1741
 Bartko, H., Martins, F., Trippe, S., et al. 2010, *ApJ*, 708, 834
 Beasor, E. R., Davies, B., Smith, N., et al. 2023, *MNRAS*, 524, 2460
 Bestenlehner, J. M. 2020, *MNRAS*, 493, 3938
 Björklund, R., Sundqvist, J. O., Puls, J., & Najarro, F. 2021, *A&A*, 648, A36
 Björklund, R., Sundqvist, J. O., Singh, S. M., Puls, J., & Najarro, F. 2023, *A&A*, 676, A109
 Calderón, D., Ballone, A., Cuadra, J., et al. 2016, *MNRAS*, 455, 4388
 Calderón, D., Cuadra, J., Russell, C. M. P., et al. 2025, *A&A*, 693, A180
 Calderón, D., Cuadra, J., Schartmann, M., et al. 2020a, *MNRAS*, 493, 447
 Calderón, D., Cuadra, J., Schartmann, M., Burkert, A., & Russell, C. M. P. 2020b, *ApJ*, 888, L2
 Choi, J., Dotter, A., Conroy, C., et al. 2016, *ApJ*, 823, 102
 Ciurlo, A., Morris, M. R., Campbell, R. D., et al. 2021, *ApJ*, 910, 143
 Costa, G., Shepherd, K. G., Bressan, A., et al. 2025, *A&A*, 694, A193
 Crowther, P. A. 2007, *ARA&A*, 45, 177
 Crowther, P. A., Hillier, D. J., & Smith, L. J. 1995a, *A&A*, 293, 172
 Crowther, P. A., Smith, L. J., & Willis, A. J. 1995b, *A&A*, 304, 269
 Cuadra, J., Nayakshin, S., & Martins, F. 2008, *MNRAS*, 383, 458
 Cuadra, J., Nayakshin, S., Springel, V., & Di Matteo, T. 2005, *MNRAS*, 360, L55
 Cuadra, J., Nayakshin, S., & Wang, Q. D. 2015, *MNRAS*, 450, 277
 Curé, M. 2004, *ApJ*, 614, 929
 Curé, M. & Rial, D. F. 2007, *Astronomische Nachrichten*, 328, 513
 Davies, B., Crowther, P. A., & Beasor, E. R. 2018, *MNRAS*, 478, 3138
 de Burgos, A., Keszhelyi, Z., Simón-Díaz, S., & Urbaneja, M. A. 2024, *A&A*, 687, L16
 de Jager, C., Nieuwenhuijzen, H., & van der Hucht, K. A. 1988, *A&AS*, 72, 259
 Decin, L., Richards, A. M. S., Marchant, P., & Sana, H. 2024, *A&A*, 681, A17
 Eggenberger, P., Meynet, G., Maeder, A., et al. 2008, *Ap&SS*, 316, 43
 Ekström, S., Georgy, C., Eggenberger, P., et al. 2012, *A&A*, 537, A146

Table 4: Time-averaged surface abundances at the different WR spectroscopic phases of our evolution models.

Spectral phase	M_{zams} [M_{\odot}]	$\Delta\tau_{\text{phase}}$ [yr]	$\langle X_{\text{H}} \rangle$	$\langle X_{\text{He}} \rangle$	mass percentage			$\log\langle \dot{M} \rangle$ [$M_{\odot} \text{ yr}^{-1}$]
					$\langle X_{\text{C}} \rangle$	$\langle X_{\text{N}} \rangle$	$\langle X_{\text{O}} \rangle$	
ZAMS, $Z = 0.020$			70.83	27.16	0.354	0.103	0.858	
Ofpe/WN9	60	8.61×10^3	21.35 ± 0.01	76.69 ± 0.01	0.013 ± 0	1.173 ± 0	0.090 ± 0	-3.91
	40	1.60×10^4	31.96 ± 2.11	66.07 ± 2.11	0.010 ± 0	1.089 ± 0.02	0.191 ± 0.02	-4.61
	32	4.44×10^4	37.27 ± 1.02	60.75 ± 1.02	0.009 ± 0	1.007 ± 0.01	0.286 ± 0.01	-5.00
	25	9.37×10^4	39.91 ± 2.38	58.04 ± 2.29	0.008 ± 0	1.022 ± 0.10	0.325 ± 0.01	-5.80
eWNL	60	4.72×10^4	18.01 ± 6.04	79.78 ± 5.39	0.035 ± 0.13	1.365 ± 0.59	0.104 ± 0.10	-4.34
	40	9.17×10^4	10.52 ± 7.00	86.88 ± 6.31	0.067 ± 0.20	1.695 ± 0.87	0.105 ± 0.07	-4.81
	32	1.35×10^5	12.30 ± 9.08	84.73 ± 8.07	0.077 ± 0.23	1.975 ± 1.21	0.146 ± 0.07	-5.14
	25	1.04×10^5	10.98 ± 8.91	80.29 ± 4.88	0.339 ± 0.72	6.062 ± 3.29	1.406 ± 1.31	-5.28
WN/C	60	4.14×10^3	0.048 ± 0.06	90.04 ± 1.63	4.176 ± 1.74	3.368 ± 0.47	1.327 ± 0.34	-3.85
	40	1.66×10^4	0.076 ± 0.07	90.15 ± 1.56	4.391 ± 1.81	3.498 ± 0.48	0.741 ± 0.21	-4.44
	32	3.06×10^4	0.009 ± 0.01	88.96 ± 1.81	5.101 ± 2.04	3.918 ± 0.55	0.780 ± 0.25	-4.80
	25	3.02×10^4	0.046 ± 0.05	75.44 ± 2.30	7.053 ± 1.98	9.111 ± 0.92	6.997 ± 1.22	-5.16
WC	60	4.48×10^4	0 ± 0	56.10 ± 15.10	30.75 ± 10.78	0.661 ± 0.60	10.43 ± 4.51	-4.16
	40	1.06×10^5	0 ± 0	62.40 ± 16.24	27.77 ± 12.27	0.959 ± 0.75	6.907 ± 4.36	-4.58
	32	1.31×10^5	0 ± 0	59.74 ± 15.32	29.49 ± 11.58	1.23 ± 0.83	7.520 ± 4.25	-4.71
	25	9.03×10^3	0 ± 0.01	36.28 ± 9.41	26.77 ± 4.62	1.03 ± 1.69	34.14 ± 6.71	-4.74

Foellmi, C., Moffat, A. F. J., & Guerrero, M. A. 2003, MNRAS, 338, 1025
 Genzel, R., Eisenhauer, F., & Gillessen, S. 2010, Reviews of Modern Physics, 82, 3121
 Georgy, C., Ekström, S., Meynet, G., et al. 2012, A&A, 542, A29
 Georgy, C., Meynet, G., & Maeder, A. 2011, A&A, 527, A52
 Georgy, C., Saio, H., & Meynet, G. 2014, MNRAS, 439, L6
 Ghez, A. M., Duchêne, G., Matthews, K., et al. 2003, ApJ, 586, L127
 Gillessen, S., Eisenhauer, F., Cuadra, J., et al. 2025, arXiv e-prints, arXiv:2510.00897
 Gillessen, S., Genzel, R., Fritz, T. K., et al. 2012, Nature, 481, 51
 Goldman, S. R., van Loon, J. T., Zijlstra, A. A., et al. 2017, MNRAS, 465, 403
 Gómez-González, V. M. A., Oskinova, L. M., Hamann, W. R., et al. 2025, A&A, 695, A197
 Gormaz-Matamala, A. C., Cuadra, J., Ekström, S., et al. 2024, A&A, 687, A290
 Gormaz-Matamala, A. C., Cuadra, J., Meynet, G., & Curé, M. 2023, A&A, 673, A109
 Gormaz-Matamala, A. C., Curé, M., Cidale, L. S., & Venero, R. O. J. 2019, ApJ, 873, 131
 Gormaz-Matamala, A. C., Curé, M., Lobel, A., et al. 2022a, A&A, 661, A51
 Gormaz-Matamala, A. C., Curé, M., Meynet, G., et al. 2022b, A&A, 665, A133
 Gormaz-Matamala, A. C., Romagnolo, A., & Belczynski, K. 2025, A&A, 696, A72
 Gräffener, G. & Hamann, W. R. 2008, A&A, 482, 945
 Groh, J. H., Meynet, G., Ekström, S., & Georgy, C. 2014, A&A, 564, A30
 Habibi, M., Gillessen, S., Martins, F., et al. 2017, ApJ, 847, 120
 Hayden, M. R., Holtzman, J. A., Bovy, J., et al. 2014, AJ, 147, 116
 Humphreys, R. M. & Jones, T. J. 2022, AJ, 163, 103
 Humphreys, R. M., Weis, K., Davidson, K., & Gordon, M. S. 2016, ApJ, 825, 64
 Hurlley, J. R., Pols, O. R., & Tout, C. A. 2000, MNRAS, 315, 543
 Josiek, J., Ekström, S., & Sander, A. A. C. 2024, A&A, 688, A71
 Josiek, J., Sander, A. A. C., Bernini-Peron, M., et al. 2025, A&A, 697, A193
 Kee, N. D., Sundqvist, J. O., Decin, L., de Koter, A., & Sana, H. 2021, A&A, 646, A180
 Krtićka, J. & Kubát, J. 2017, A&A, 606, A31
 Krtićka, J. & Kubát, J. 2018, A&A, 612, A20
 Krtićka, J., Kubát, J., & Krtićková, I. 2021, A&A, 647, A28
 Krtićka, J., Kubát, J., & Krtićková, I. 2024, A&A, 681, A29
 Kruckow, M. U., Andrews, J. J., Fragos, T., et al. 2024, A&A, 692, A141
 Labaj, M., Ressler, S. M., Zajaček, M., et al. 2025, A&A, 702, A233
 Liu, B., Sibony, Y., Meynet, G., & Bromm, V. 2025, ApJ, 980, L30
 Lu, J. R., Do, T., Ghez, A. M., et al. 2013, ApJ, 764, 155
 Maeder, A. 1987, A&A, 178, 159
 Maeder, A. 1997, A&A, 321, 134
 Maeder, A. & Meynet, G. 2000, A&A, 361, 159
 Maeder, A., Przybilla, N., Nieva, M.-F., et al. 2014, A&A, 565, A39
 Mapelli, M. & Gualandris, A. 2016, in Lecture Notes in Physics, Berlin Springer Verlag, ed. F. Haardt, V. Gorini, U. Moschella, A. Treves, & M. Colpi, Vol. 905, 205
 Martinet, S., Meynet, G., Ekström, S., Georgy, C., & Hirschi, R. 2023, A&A, 679, A137

Martins, F., Genzel, R., Hillier, D. J., et al. 2007, A&A, 468, 233
 McDonald, S. L. E., Davies, B., & Beasor, E. R. 2022, MNRAS, 510, 3132
 Meynet, G., Chomienne, V., Ekström, S., et al. 2015, A&A, 575, A60
 Meynet, G., Ekstrom, S., Maeder, A., et al. 2013, in Lecture Notes in Physics, Berlin Springer Verlag, ed. M. Goupil, K. Belkacem, C. Neiner, F. Lignières, & J. J. Green, Vol. 865, 3
 Meynet, G. & Maeder, A. 2003, A&A, 404, 975
 Meynet, G. & Maeder, A. 2005, A&A, 429, 581
 Murchikova, E. M., Phinney, E. S., Panoast, A., & Blandford, R. D. 2019, Nature, 570, 83
 Nandal, D., Meynet, G., Ekström, S., et al. 2024, A&A, 684, A169
 Nayakshin, S., Dehnen, W., Cuadra, J., & Genzel, R. 2006, MNRAS, 366, 1410
 Nugis, T. & Lamers, H. J. G. L. M. 2000, A&A, 360, 227
 Pauldrach, A. W. A. & Puls, J. 1990, A&A, 237, 409
 Paumard, T., Genzel, R., Martins, F., et al. 2006, ApJ, 643, 1011
 Paxton, B., Bildsten, L., Dotter, A., et al. 2011, ApJS, 192, 3
 Przybilla, N., Firmstein, M., Nieva, M. F., Meynet, G., & Maeder, A. 2010, A&A, 517, A38
 Quataert, E. 2004, ApJ, 613, 322
 Ressler, S. M., Quataert, E., & Stone, J. M. 2018, MNRAS, 478, 3544
 Ressler, S. M., Quataert, E., & Stone, J. M. 2020, MNRAS, 492, 3272
 Romagnolo, A., Gormaz-Matamala, A. C., & Belczynski, K. 2024, ApJ, 964, L23
 Russell, C. M. P., Wang, Q. D., & Cuadra, J. 2017, MNRAS, 464, 4958
 Sander, A. A. C., Lefever, R. R., Poniatowski, L. G., et al. 2023, A&A, 670, A83
 Sander, A. A. C. & Vink, J. S. 2020, MNRAS, 499, 873
 Schödel, R., Ott, T., Genzel, R., et al. 2002, Nature, 419, 694
 Sibony, Y., Georgy, C., Ekström, S., & Meynet, G. 2023, A&A, 680, A101
 Smith, L. F., Shara, M. M., & Moffat, A. F. J. 1996, MNRAS, 281, 163
 Szécsi, D., Agrawal, P., Wünsch, R., & Langer, N. 2022, A&A, 658, A125
 van Loon, J. T. 2025, Galaxies, 13, 72
 Venero, R. O. J., Curé, M., Puls, J., et al. 2024, MNRAS, 527, 93
 Verhamme, O., Sundqvist, J., de Koter, A., et al. 2024, A&A, 692, A91
 Vink, J. S., de Koter, A., & Lamers, H. J. G. L. M. 1999, A&A, 350, 181
 Vink, J. S., de Koter, A., & Lamers, H. J. G. L. M. 2001, A&A, 369, 574
 von Fellenberg, S. D., Gillessen, S., Stadler, J., et al. 2022, ApJ, 932, L6
 Wang, Q. D., Li, J., Russell, C. M. P., & Cuadra, J. 2020, MNRAS, 492, 2481
 Yang, M., Bonanos, A. Z., Jiang, B., et al. 2023, A&A, 676, A84
 Yusof, N., Hirschi, R., Eggenberger, P., et al. 2022, MNRAS, 511, 2814
 Zahn, J. P. 1992, A&A, 265, 115
 Zapartas, E., de Wit, S., Antoniadis, K., et al. 2025, A&A, 697, A167

Appendix A: Mass-loss rate recipes

For the winds of OB-type stars ($T_{\text{eff}} \geq 10$ kK) we use the formula from Krtićka et al. (2024, Eq. 3 with coefficients from Table 3)

$$\log \dot{M}_{\text{K24}} = -13.82 + 0.358 \log \left(\frac{Z}{Z_{\odot}} \right) + \log \left(\frac{L_*}{10^6 L_{\odot}} \right) \times \left[1.52 - 0.11 \log \left(\frac{Z}{Z_{\odot}} \right) \right] \\ + 13.82 \log \left\{ \left[1.0 + 0.73 \log \left(\frac{Z}{Z_{\odot}} \right) \right] \exp \left[-\frac{(T_{\text{eff}}/\text{kK} - 14.16)^2}{3.58^2} \right] + 3.84 \exp \left[-\frac{(T_{\text{eff}}/\text{kK} - 37.9)^2}{56.5^2} \right] \right\}. \quad (\text{A.1})$$

For the mass-loss rate of stars in the range of temperatures between 5 and 10 kK we use the linearised formula of de Jager et al. (1988)

$$\log \dot{M}_{\text{dJ88}} = -8.158 + 1.769 \log \left(\frac{L_*}{L_{\odot}} \right) - 1.676 \log T_{\text{eff}}. \quad (\text{A.2})$$

For the mass-loss rate of red supergiants ($T_{\text{eff}} \leq 5$ kK) we use the formula of Yang et al. (2023)

$$\log \dot{M}_{\text{Y23}} = 0.45 \left[\log \left(\frac{L_*}{L_{\odot}} \right) \right]^3 - 5.26 \left[\log \left(\frac{L_*}{L_{\odot}} \right) \right]^2 + 20.93 \log \left(\frac{L_*}{L_{\odot}} \right) - 34.56. \quad (\text{A.3})$$

For the wind of Wolf-Rayet stars with $T_* \leq 70$ kK we use Gräfener & Hamann (2008)

$$\log \dot{M}_{\text{GH08}} = 10.046 + \beta \log(\Gamma_e - \Gamma_0) - 3.5 \log(T_*/\text{kK}) + 0.42 \log \left(\frac{L_*}{L_{\odot}} \right) - 0.45 X_{\text{H}}, \quad (\text{A.4})$$

with

$$\beta(Z) = 1.727 + 0.25 \log \left(\frac{Z}{Z_{\odot}} \right),$$

$$\Gamma_0(Z) = 0.325 - 0.301 \log \left(\frac{Z}{Z_{\odot}} \right) - 0.045 \left[\log \left(\frac{Z}{Z_{\odot}} \right) \right]^2.$$

Finally, for Wolf-Rayet stars out of the range covered by Gräfener & Hamann (2008), we use the formulae from Nugis & Lamers (2000) for WN and WC/WO phases

$$\log \dot{M}_{\text{NL00,WN}} = -13.6 + 1.63 \log \left(\frac{L_*}{L_{\odot}} \right) + 2.22 \log Y_{\text{He}}, \quad (\text{A.5})$$

$$\log \dot{M}_{\text{NL00,WC/WO}} = -8.30 + 0.84 \log \left(\frac{L_*}{L_{\odot}} \right) + 2.04 \log Y_{\text{He}} + 1.04 \log \left(\frac{Z}{Z_{\odot}} \right). \quad (\text{A.6})$$